Draft version August 15, 2019
Preprint typeset using LaTeX style emulateapj v. 12/16/11

THE ACCRETION HISTORY OF AGN: A NEWLY DEFINED POPULATION OF COLD QUASARS

Allison Kirkpatrick[1], C. Megan Urry[2,3], Jason Brewster[4], Kevin C. Cooke[5], Michael Estrada[1], Eilat Glikman[6], Kurt Hamblin[4], Tonima Tasnim Ananna[2,3], Casey Carlile[1], Brandon Coleman[1], Jordan Johnson[1], Jeyhan S. Kartaltepe[5], Stephanie M. LaMassa[7], Stefano Marchesi[8], Meredith Powell[2,3,9], Dave Sanders[10], Ezequiel Treister[11], Tracey Jane Turner[4,12]

Draft version August 15, 2019

ABSTRACT

Quasars are the most luminous of active galactic nuclei (AGN), and are perhaps responsible for quenching star formation in their hosts. The Stripe 82X catalog covers 31.3 deg^2 of the Stripe 82 field, of which the 15.6 deg^2 covered with *XMM-Newton* is also covered by *Herschel*/SPIRE. We have 2500 X-ray detected sources with multi-wavelength counterparts, and 30% of these are unobscured quasars, with $L_X > 10^{44}$ erg/s and $M_B < -23$. We define a new population of quasars which are unobscured, have X-ray luminosities in excess of 10^{44} erg/s, have broad emission lines, and yet are also bright in the far-infrared, with a 250 μm flux density of $S_{250} > 30$ mJy. We refer to these *Herschel*-detected, unobscured quasars as "Cold Quasars". A mere 4% (23) of the X-ray- and optically-selected unobscured quasars in Stripe 82X are detected at 250 μm. These Cold Quasars lie at $z \sim 1-3$, have $M_{\rm dust} \sim 10^8 - 10^9\, M_\odot$, have $L_{\rm IR} > 10^{12}\, L_\odot$, and have star formation rates of $200-2000\, M_\odot$/yr. Cold Quasars are bluer in the mid-IR than the full quasar population, and 75% of our Cold Quasars have *WISE* W3 < 11.5 [Vega], while only 19% of the full quasar sample meets this criteria. Crucially, Cold Quasars have $4-7\times$ as much star formation as the unobscured quasar population at similar redshifts. This phase is likely short-lived, as the central engine and immense star formation consume the gas reservoir. Cold Quasars are type-1 blue quasars that reside in starburst galaxies.

1. INTRODUCTION

The origin of luminous quasars is perhaps a dramatic story, wherein two immense galaxies collide, fueling a burst of star formation and triggering rapid growth of a supermassive black hole (e.g., Hopkins et al. 2006). In the major merger paradigm, the active galactic nucleus (AGN) goes through an obscured growth phase, where the accretion disk is hidden by dust, while the host galaxy experiences a period of enhanced star formation. This phase ends when the AGN launches winds powerful enough to blow away some of the circumnuclear obscuring dust so that the accretion disk becomes visible in the optical as star formation quenches in the host galaxy (Glikman et al. 2004, 2012; Pontzen & Governato 2012). Quasars are the most luminous of AGN, and it has been suggested that they are almost universally produced by major mergers (Treister et al. 2012).

AGN can heat torus and circumnuclear dust to >1000 K, producing an IR SED that emits a power-law from $\lambda = 1-40\mu$m (e.g., Elvis et al. 1994; Netzer et al. 2007; Mullaney et al. 2011). Additionally, AGN heat and excite physically extended gas clouds to form the narrow line region, which in extreme cases of merging galaxies can be larger than the galaxy itself (e.g., Hainline et al. 2016). The narrow line region contains gas ionized by the radiation field of the AGN, and it also contains dust (Groves et al. 2006). Nebular dust emission typically peaks around 25 μm, although the exact temperature depends on the incident radiation field and optical depth. In AGN where the central nucleus has a lot of obscuring material, galactic dust can be even colder, peaking at wavelengths longer than 25 μm, as the incident radiation field is absorbed and re-radiated through large column densities. It is possible, in heavily obscured cases, that the AGN can account for all of the far-IR emission (Sajina et al. 2012; Ricci et al. 2017a). Such heavily obscured objects are thought to be rare, as the amount of obscuration increases with stellar mass (Buchner et al. 2017; Buchner & Bauer 2017). In the major merger paradigm, heavily obscured phases are likely short lived (20% of the blue quasar phase), occurring briefly as the quasar is in the transitional blowout phase, after which it becomes optically luminous (Glikman et al. 2012). The quasar lifetime is only weakly constrained through clustering measurements to be $\sim 10^6 - 10^9$ yr (Conroy & White 2013; La Plante & Trac 2016)

The location of the obscuration in quasars produced

[1] Department of Physics & Astronomy, University of Kansas, Lawrence, KS 66045, USA, akirkpatrick@ku.edu
[2] Yale Center for Astronomy & Astrophysics, New Haven, CT 06520, USA
[3] Department of Physics, Yale University, PO BOX 201820, New Haven, CT 06520, USA
[4] Department of Physics, University of Maryland Baltimore County, Baltimore, MD 21250, USA
[5] School of Physics and Astronomy, Rochester Institute of Technology, Rochester, NY 14623, USA
[6] Department of Physics, Middlebury College, Middlebury, VT 05753, USA
[7] Space Telescope Science Institute, 3700 San Martin Dr, Baltimore, MD 21218, USA
[8] INAF - Osservatorio di Astrofisica e Scienza dello Spazio di Bologna, Via Piero Gobetti, 93/3, 40129, Bologna, Italy
[9] Kavli Institute for Particle Astrophysics and Cosmology, Stanford University, 452 Lomita Mall, Stanford, CA 94305, USA
[10] Institute for Astronomy, University of Hawaii, 2680 Woodlawn Drive, Honolulu, HI 96822, USA
[11] Instituto de Astrofísica, Facultad de Física, Pontificia Universidad Católica de Chile, Casilla 306, Santiago 22, Chile
[12] Center for Space Science and Technology, University of Maryland Baltimore County, 1000 Hilltop Circle, Baltimore, MD 21250, USA

by mergers is difficult to tease out, as it can in principal arise from any dust or gas along the line of sight. The traditional torus model places the obscurer in a compact, donut-like structure within a few parsecs of the accretion disk. In the most successful torus models, the torus does not have sharp edges, is physically related to the accretion disk, and is made of clumpy clouds of dust and gas (e.g., Elitzur & Shlosman 2006). Obscured AGN can be the product of a viewing angle through the thicker parts of the torus (Urry & Padovani 1995). The torus is structurally related to the supermassive black hole by being under its gravitational influence, absorbing radiation from the accretion disk, and possibly being formed from winds off of the accretion disk. The host galaxy itself is another source of obscuration. Gas and dust in the host galaxy are not associated with the AGN structure, even if they are circumnuclear. Buchner et al. (2017) and Buchner & Bauer (2017) measured hydrogen column densities from the host galaxy and the AGN and found that the galaxy can account for Compton thin obscuration ($N_H = 10^{22}\,\mathrm{cm}^{-2}$) but not Compton thick ($N_H > 10^{24}\,\mathrm{cm}^{-2}$). Dust absorption is commonly parameterized by the optical depth of the 9.7 μm silicate absorption feature (Spoon et al. 2007). High silicate optical depth is observed in obscured AGN, and this dust may arise from the torus (Hatziminaoglou et al. 2015). In local mergers, Goulding et al. (2012) showed that silicate dust absorption correlates with the viewing angle of the host galaxy and not with gas column densities of the AGN measured from the X-ray. Dust and gas obscuration can arise from a foreground screen rather than the AGN structure itself (Hatziminaoglou et al. 2015; Buchner et al. 2017). In fact, mergers in particular exhibit a clear correlation between gas and dust obscuration and merger stage, with late stage mergers being more obscured (Sanders & Mirabel 1996; Hopkins et al. 2008; Petric et al. 2011; Stierwalt et al. 2013; Ricci et al. 2017a).

Quasars may substantially affect the star formation of their host galaxies through feedback processes, though the exact nature of that role remains unclear. In AGN, winds can either blow out the interstellar medium and quench star formation (negative feedback; Hopkins et al. 2006), or they can compress the interstellar medium and trigger star formation (positive feedback; Ciotti & Ostriker 2007). Accretion onto the most massive black holes is observed to produce collimated jets that sweep through the galaxy producing kinetic feedback (Heckman & Best 2014). However, in a limited number of sources, star formation is observed to be enhanced in X-ray-selected and optically-selected AGN (Salomé et al. 2015; Mahoro et al. 2017; Perna et al. 2018). Further complicating matters, other studies indicate no link between AGN activity and either enhanced or decreased star formation. For example, Stanley et al. (2017) find no decrease in star formation rate (SFR) with AGN bolometric luminosity for the optically-selected AGN from the Sloan Digital Sky Survey (SDSS). Recently, Schulze et al. (2019) found that 20 unobscured quasars at $z \sim 2$ have no statistically significant difference in SFRs than star-forming galaxies, based on ALMA continuum measurements. In a small local sample, unobscured quasars were shown to have similar dust masses as obscured quasars, indicating that unobscured quasars might not be in a later evolutionary stage (Shangguan & Ho 2019).

One problem in synthesizing literature results into a coherent picture is that selection in different wavelength regimes can produce biased samples (Hickox et al. 2009; Azadi et al. 2017), particularly when studying obscured AGN. As 75% of AGN growth is obscured (Treister et al. 2004; Ananna et al. 2019), these sources provide the most insight into black hole—galaxy coevolution. Unobscured AGN, and in particular quasars, should provide the clearest insight into how massive galaxies die, as unobscured quasars have presumably blown out their own obscuring material. Their immense energies should start to affect their hosts and usher in the passive galaxy phase. But making this connection directly is hard. Precisely because unobscured quasars are so luminous, it becomes very difficult to study their host galaxy properties. Quasars outshine their hosts in the optical and mid-IR photometry (Hainline et al. 2011; Stern et al. 2012). They contaminate the optical emission lines used to study star formation, particularly H_α (Baldwin et al. 1981). Submillimeter emission lines, which trace the dense interstellar medium (ISM) in star-forming regions, are also enhanced in AGN (Imanishi et al. 2016; Kamenetzky et al. 2016; Kirkpatrick et al. 2019). The most robust tracer of the host galaxy is therefore the far-IR, as AGN are expected not to be able to heat dust beyond $\lambda > 100\mu$m, as is evidenced by the sharp drop in far-IR emission seen in X-ray luminous AGN (Mullaney et al. 2011; Rosario et al. 2012). Lyu & Rieke (2017) argue that AGN in fact cannot account for much emission at wavelengths longer than 20 μm, simply due to energy balance arguments.

In this paper, we present an unbiased look at the interstellar medium of unobscured quasars. This is the first in a series of papers examining in detail the multi-wavelength emission of X-ray selected AGN with far-IR emission in the Accretion History of AGN survey (AHA[13]; PI, M. Urry). We discuss the survey and infrared sample selection in Section 2, including our definition of Cold Quasars. We discuss in Section 3 how the IR emission of Cold Quasars compares with unobscured quasars. Our conclusions are listed in Section 4. Throughout this paper, we assume a standard cosmology with $H_0 = 70\,\mathrm{km\,s^{-1}\,Mpc^{-1}}$, $\Omega_\mathrm{M} = 0.3$ and $\Omega_\Lambda = 0.7$.

2. A MULTI-WAVELENGTH AGN SURVEY

Large volumes of the universe must be surveyed in order to discover a representative sample of rare objects like high-luminosity AGN. This paper is part of AHA, which is a multi-wavelength survey that assembles data from the Stripe 82X (31 deg^2; LaMassa et al. 2013a,b, 2015), COSMOS (2 deg^2; Cappelluti et al. 2007; Scoville et al. 2007; Elvis et al. 2009; Civano et al. 2016; Marchesi et al. 2016), and GOODS-South fields (0.1 deg^2; Brandt et al. 2001; Giacconi et al. 2002; Giavalisco et al. 2004). These fields comprise a "wedding cake" tiered X-ray survey, where each cake layer probes a different area and flux limit, and thus a different luminosity-redshift range. Stripe 82X covers the most luminous sources, while COSMOS and GOODS-South contain less luminous and/or more obscured AGN. We focus here on the Stripe 82X

[13] http://project.ifa.hawaii.edu/aha/

component, which has the most luminous X-ray sources in our survey and will discuss the IR AGN in the full AHA survey in a subsequent paper.

Our team surveyed 4.6 deg^2 and 15.6 deg^2 of the Sloan Digital Sky Survey (SDSS) field Stripe 82 with *XMM-Newton* in AO10 and AO13 (LaMassa et al. 2013c, 2016). We combined these observations with a further 5.6 deg^2 of *XMM-Newton* archival pointings and 6.0 deg^2 of *Chandra* archival pointings in Stripe 82 for a total Stripe 82X survey area of 31.3 deg^2. From this catalog, 15.6 deg^2, covered with *XMM-Newton* in AO13, is also fully covered by *Herschel Space Observatory* observations with the SPIRE instrument as part of the *Herschel* Stripe82 Survey (HerS; Viero et al. 2014). AO13 has coadded exposure times of 6–8 ks (LaMassa et al. 2016). Additionally, there are 125 sources from AO10 that fall in the HerS survey region (LaMassa et al. 2013c). We refer the reader to Figure 1 in Ananna et al. (2017) for the layout of Stripe 82 covered by *XMM* and *Herschel*. Multi-wavelength counterpart matching was done in LaMassa et al. (2016) and Ananna et al. (2017). The authors use the co-added SDSS catalogs (Jiang et al. 2014; Fliri & Trujillo 2016), which reach 2.5 mag deeper than single epoch data, to increase the likelihood of each X-ray source having an optical counterpart. The authors match the X-ray positions to multi-wavelength counterparts spanning the UV to the mid-IR. This portion of Stripe 82 is covered by warm *Spitzer* (3.6 & 4.5 μm only) through the *Spitzer*/HETDEX Exploratory Large Area (SHELA) survey (Papovich et al. 2016), the *Spitzer* IRAC Equatorial Survey (SpIES; Timlin et al. 2016), and by *WISE* in the mid-IR. It is also covered in the near-IR by the Vista Hemisphere Survey (McMahon et al. 2013) and the UKIRT Infrared Deep Sky Survey (Lawrence et al. 2007), and in the UV by *GALEX*. Full details of the observations and counterpart identification can be found in LaMassa et al. (2016) and Ananna et al. (2017). The 16 deg^2 portion of Stripe 82X that overlaps with the HerS survey area contains 3200 X-ray sources (LaMassa et al. 2016). We remove 295 sources that do not have robust multi-wavelength counterparts (and hence photo-zs), as indicated by a counterpart quality flag of 3 or 4 in the Ananna et al. (2017) photometric catalog. This leaves 2905 X-ray sources.

2.1. *The Herschel/X-ray Subsample*

One of the goals of AHA is to determine the host galaxy properties of the most luminous X-ray sources. This requires unambiguous observations of the host galaxy, which, for unobscured AGN, can best be done at longer wavelengths, such as the far-IR and sub-mm. A luminous AGN can contaminate all other wavelengths. Of the 2905 X-ray sources, 120 galaxies are also detected at 250 μm, which we refer to as the *Herschel* subsample. The HerS survey has a 3σ detection limit of $S_{250\,\mu\mathrm{m}} = 30$ mJy (Viero et al. 2014). In a purely star-forming galaxy, this flux detection limit corresponds to an SFR of 174 $M_\odot$/yr at $z = 1$ and 758 $M_\odot$/yr at $z = 2$, estimated using the Kirkpatrick et al. (2012) templates. We summarize the sample selection Figure 1.

Ninety-nine galaxies from the *Herschel* subsample have spectroscopic redshifts measured from SDSS spectra (from DR12, DR13, or DR14). The remaining 21

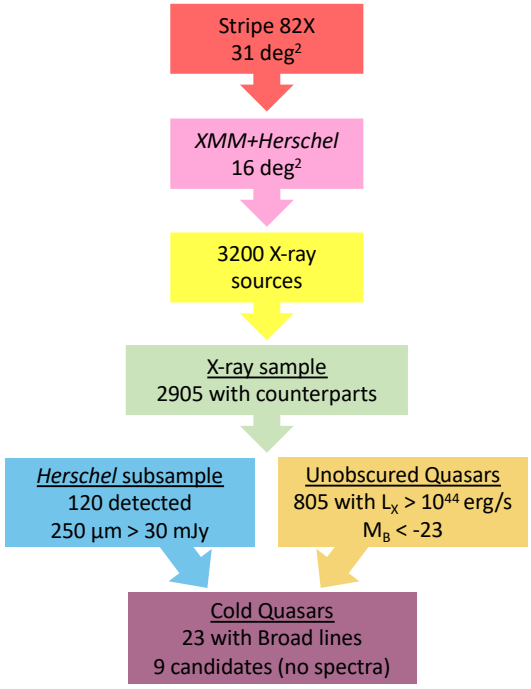

FIG. 1.— Visual summary of our main sample selection criteria.

have photometric redshifts determined by fitting the UV/optical/NIR data with the LePhare code (Arnouts et al. 1999; Ilbert et al. 2006). We show the full band X-ray luminosity (throughout the text, $L_X = L_{0.5-10\,\mathrm{kev}}$) and redshift distribution of the Stripe 82X sources and *Herschel* subsample in Figure 2. The X-ray luminosities have been k-corrected using $\Gamma = 2.0$ for the hard band and $\Gamma = 1.8$ for the soft band (LaMassa et al. 2016), but they are not corrected for absorption.

2.2. *Cold Quasar Definition*

We find that many of our *Herschel* subsample are unobscured, luminous AGN. We call unobscured quasars any source with $L_X > 1 \times 10^{44}$ erg/s and $M_B < -23$ (Schmidt & Green 1983; McDowell et al. 1989). To transform between the SDSS filters and the B band, we used the equation

$$m_B = m_g + 0.17(m_u - m_g) + 0.11 \quad (1)$$

(Jester et al. 2005). From the full X-ray sample, 805 sources meet this definition. We refer to these as the unobscured quasars throughout the text and figures. Of the *Herschel* subsample, 32 galaxies satisfy these criteria, 23 of which have optical broad lines, confirming that they are type-1 quasars. Herein, we create a new definition to categorize quasars. We refer to these 23 galaxies as the "Cold Quasars". The remaining nine *Herschel* sources either do not have an SDSS spectrum or have a spectrum with low signal to noise ratio, making it difficult to distinguish broad lines. We refer to these nine galaxies as Cold Quasar Candidates throughout the text. We will analyze all optical spectra from the full *Herschel* subsample in a future paper (Estrada et al., in prep).

All Cold Quasars resemble point sources in the optical and are unresolved in the *Herschel* bands (Figures

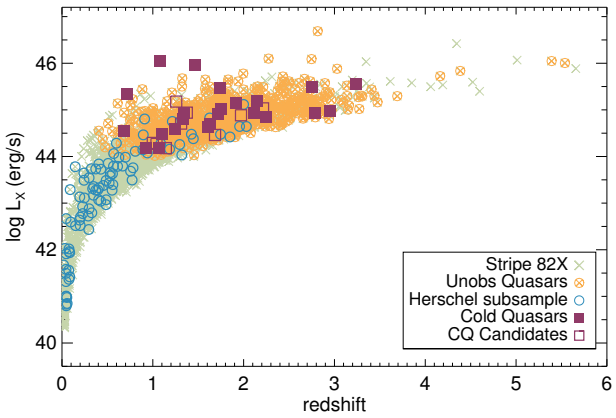

FIG. 2.— The X-ray ($0.5-10$ kev) luminosity and redshift distribution of the full Stripe 82X sample in the 16 deg^2 region of the sky covered by both *XMM-Newton* and *Herschel* (light green crosses; 2905 galaxies). The 120 galaxies detected in both the X-ray and at 250 μm form our *Herschel* subsample (blue circles). We refer to the X-ray sources with $L_X > 1\times10^{44}$ erg/s and $M_B < -23$ as unobscured quasars (orange circles with crosses). The unobscured quasars with a 250 μm detection are our Cold Quasar subsample (purple filled squares). We identify Cold Quasar candidates as sources that meet the stated definitions but lack optical broad-line emission, either due to not having a spectrum or having a spectrum with a low signal-to-noise ratio.

3 and 4). We show all optical and *Herschel* images on our website (https://kirkpatrick.ku.edu/CQ/). [14] They lie between $0.5 < z < 3.5$, due to the extreme X-ray luminosities. We list the properties of the Cold Quasars in Table 1. All Cold Quasars are detected in all three *Herschel*/SPIRE bands.

Red Quasars are type-1 quasars that have a red continuum in the optical, indicating a moderate amount of dust ($E(B-V) > 0.25$) along the line of sight that does not fully obscure the broad-line region (Urrutia et al. 2008; Glikman et al. 2013, 2018). These quasars are among the most luminous objects in the universe and are generally found in late-stage mergers (Glikman et al. 2015). Red Quasar candidates can be selected using $r_{\rm AB}-K_{\rm Vega} > 5 \wedge J-K > 1.5$ (Glikman et al. 2013). According to this color selection, none of our Cold Quasars or Cold Quasar candidates are Red Quasars. We find the Cold Quasar population is distinct from the Red Quasar population in that they do not have reddened continua.

2.3. *Host Galaxy Properties*

We determined the infrared luminosities and IR AGN contribution of all *Herschel* X-ray sources using the spectral decomposition code SED3FIT (Berta et al. 2013), assuming the default set of models. SED3FIT fits the UV–far-IR for galaxies assuming an energy balance model. The galaxy stellar and dust components come from the MAGPHYS code (da Cunha et al. 2008). MAGPHYS couples the stellar library of Bruzual & Charlot (2003) with mid- and far-IR dust emission that depends on the UV/optical attenuation. The AGN SEDs, from the Fritz et al. (2006) models, consists of isotropic emission of the central source, which is assumed to be point-like. This emission is composed of power laws in the wavelength range of $0.001-20\mu$m. The second component is radiation from dust with a toroidal geometry. The torus models take into account a range of dust geometries and radii. Part of the direct emission of the AGN is either absorbed by the toroidal obscurer and re-emitted at longer wavelengths ($1-1000\,\mu$m) or scattered by the same medium. The default set of models includes 10 torus models and randomly samples the optical/IR library 1000 times, as it is computationally prohibitive to fit the entire library of optical/IR models.

We obtained acceptable fits for 105 of the *Herschel* subsample, including 17 Cold Quasars. For the remaining 15 sources, the SED3FIT model does not fit the far-IR, with reduced $\chi^2 > 20$. We also fit all *Herschel* sources with an alternate SED decomposition code, AGNFITTER (Calistro Rivera et al. 2016). AGNFITTER simultenously fits an accretion disk, stellar population, torus, and ISM dust model to the UV–IR photometry using a Bayesian approach. However, it does not require energy balance to allow for either noisy UV/optical or IR data. The accretion disk is represented as a fixed blackbody whose normalization and $E(B-V)$ is allowed to vary. The torus models are all consistent in power law slope in the mid-IR and falling off after $\lambda > 30\,\mu$m, although the slope of the near-IR can be modified by a dust column density. These models are empirically derived from Seyfert galaxies (Silva et al. 2004). In general, the fits with AGNFITTER were worse, such that we only obtained acceptable fits for 78 sources. We obtain acceptable AGNFITTER results for nine galaxies not fit well by SED3FIT, including four Cold Quasars. For the remaining six galaxies, including one Cold Quasar, AGNFITTER also failed to accurately reproduce the far-IR emission.

We list the host galaxy properties IR luminosity ($L_{\rm IR}[8-1000\,\mu{\rm m}]$), stellar mass ($M_*$), dust mass ($M_{\rm dust}$), fraction of $L_{\rm IR}$ arising from AGN ($f_{\rm AGN}[8-1000\,\mu{\rm m}]$), and SFR in Table 1. AGNFITTER does not calculate a dust mass, so we do not list it for the four galaxies fit with that code. We did not obtain a good fit for quasar 4252 with either SED3FIT or AGNFITTER, so we do not list any host galaxy properties for it. SFR is determined by first removing the AGN contribution, $f_{\rm AGN}$, from $L_{\rm IR}$. Although we list the M_* output from the fitting codes in Table 1, we caution the reader that stellar masses are notoriously difficult to determine in type-1 quasars, due to the quasar light contaminating the optical galaxy emission.

3. RESULTS & DISCUSSION

3.1. *Infrared Colors*

Mid-IR color-color diagrams are an effective way of identifying luminous AGN (Lacy et al. 2004; Stern et al. 2005; Donley et al. 2012; Mateos et al. 2012; Stern et al. 2012). The AGN typically has a torus that radiates as a power-law, producing redder mid-IR colors than purely star-forming galaxies (Donley et al. 2012). Twenty Cold Quasars are detected in the $W1$ and $W2$ bands, and all of these meet the WISE AGN selection

[14] We use the DESI Legacy Imaging Surveys (Dey et al. 2019) to create optical images from the *grz* bands of our Cold Quasars. Our sources lie in the footprint covered by the Dark Energy Camera Legacy Survey (Flaugher et al. 2015), observed by the Dark Energy Camera on the 4-m Blanco telescope at the Cerro Tololo Inter-American Observatory. The Legacy Surveys reach a z-band limiting magnitude of 22.5 mag, making them deeper than the images in the SDSS Data Releases. However, we do not use the photometry from the Legacy Surveys for any spectral fitting or analysis.

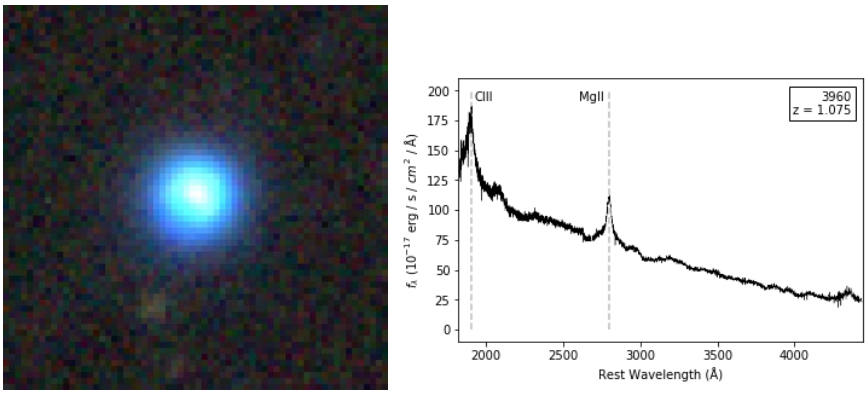

FIG. 3.— An example of a Cold Quasar (ID 3960, $z = 1.075$). *Left*–An RGB image, where blue is the g-band filter from the DECam Legacy Survey, green is the r-band, and red is the z-band. Each side of the image is 20". The blue color indicates that this quasar is not dust reddened. All of our Cold Quasars are blue point sources. *Right*–Rest frame optical SDSS spectrum with the broad-lines labeled. The continuum is blue two broad-lines are evident. Spectra and images for all *Herschel* sources are available at https://kirkpatrick.ku.edu/CQ/.

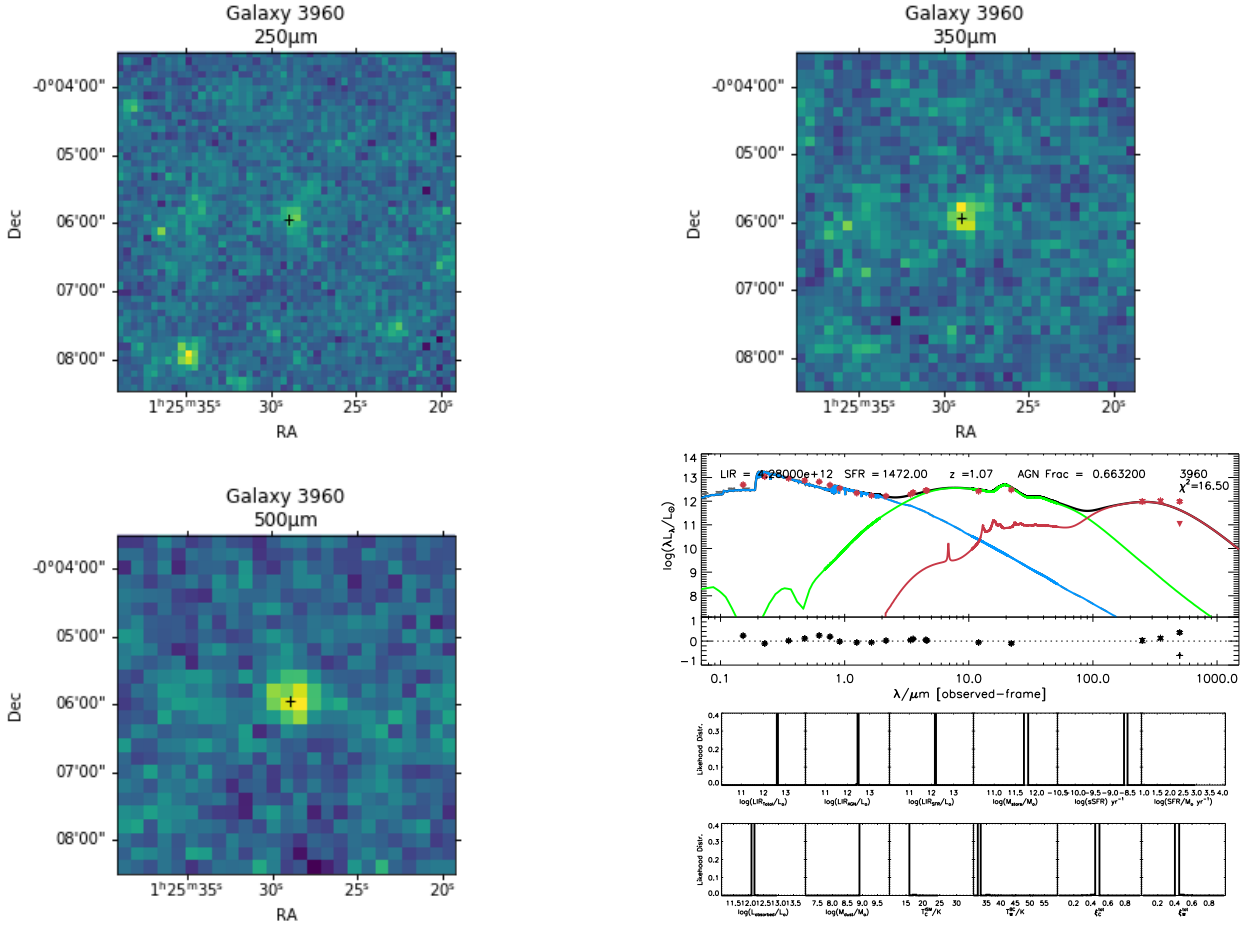

FIG. 4.— The far-IR emission of Cold Quasar 3960 ($z = 1.075$). From top to bottom, we show the 250 μm, 350 μ, and 500 μm images, with the X-ray position marked with the cross. In the bottom right, we show the SED3FIT decomposition of the SED, where blue is the stellar population, green is the torus, and red is the dust emission.

TABLE 1
Cold Quasar Properties

ID[a]	RA (J2000)	Dec (J2000)	z	$\log L_{0.5-10\,\mathrm{kev}}$ (erg/s)	$\log L_{\mathrm{IR}}(L_\odot)$	$\log M_*(M_\odot)$[b]	$\log M_{\mathrm{dust}}(M_\odot)$[c]	f_{AGN}[d]	SFR ($M_\odot$/yr)
475	01:19:48.4	+00:43:54.28	1.754	45.01	13.17±0.02	11.73	9.27±0.01	0.20	1882
507	01:59:37.8	+00:26:39.91	1.606	44.64	12.50±0.02	10.81	9.26±0.01	0.19	427
2435	00:57:43.7	-00:11:57.92	1.067	44.19	12.44±0.05	10.74	9.37±0.01	0.09	394
2480	00:58:28.9	+00:13:45.25	1.239	44.59	12.16±0.38	10.09	8.75±0.66	0.15	194
2509	00:59:05.4	+00:06:50.24	0.719	45.34	12.31±0.06	10.90	8.99±0.09	0.41	191
2551	00:59:46.6	+00:02:54.61	0.682	44.54	12.86±0.12	10.03	···	0.78	218
2651	01:01:13.3	-00:29:45.20	1.337	44.80	12.83±0.01	11.17	8.94±0.01	0.07	1009
3122	01:09:01.0	+00:01:37.44	2.955	44.98	13.21±0.05	11.46	9.00±0.01	0.01	2545
3716	01:19:00.4	-00:01:57.68	2.750	45.50	13.29±0.02	11.59	9.35±0.01	0.36	1969
3819	01:21:10.0	-00:29:10.36	1.719	44.92	12.23±0.01	11.22	9.06±0.01	0.04	257
3871	01:22:49.7	-00:07:07.13	1.631	44.71	13.25±0.21	8.32	···	0.63	1037
3960	01:25:29.0	-00:05:56.56	1.075	46.04	12.63±0.01	11.71	9.93±0.01	0.66	229
4077	01:30:34.0	-00:21:06.61	3.234	45.55	12.64±0.02	11.31	9.44±0.06	0.02	681
4252[e]	01:35:54.4	-00:22:31.91	2.249	44.85	···	···	···	···	···
4285	01:37:26.4	+00:11:52.45	1.103	44.47	13.28±0.40	10.73	···	0.86	431
4324	01:38:14.7	+00:00:05.78	2.144	45.20	12.60±0.01	10.91	9.18±0.01	0.18	519
4336	01:38:25.3	-00:05:34.39	1.341	44.94	12.95±0.01	11.34	9.60±0.01	0.20	1147
4472	01:40:33.8	+00:02:30.05	1.921	45.15	13.12±0.01	11.19	8.70±0.01	0.01	2065
4668	01:43:01.9	-00:26:56.54	2.786	44.93	12.62±0.01	11.68	9.18±0.12	0.01	657
4979	01:08:21.1	-00:02:28.51	0.930	44.19	13.19±0.32	11.08	···	0.89	276
5074	01:49:40.2	+00:17:17.76	1.464	45.95	12.41±0.02	10.68	9.32±0.01	0.39	250
5097	01:49:58.3	-00:30:25.00	2.111	44.94	12.72±0.01	10.99	9.44±0.01	0.26	622
5122	01:50:34.5	-00:02:00.46	1.740	45.47	13.26±0.01	11.76	9.39±0.01	0.10	2626

[a] The ID is the Rec_No from LaMassa et al. (2016).
[b] The uncertainties on M_* output by Sed3Fit for many of our sources were suspiciously small, so we do not quote them. In general, M_* is very difficult to determine in unobscured quasars and should be treated with a healthy dose of skepticism.
[c] Sources without a dust mass were fit with AGNFitter, as this code does not calculate M_{dust}.
[d] The fraction of IR (8–1000 μm) emission attributable to the AGN component, assuming the AGN emission is confined to the torus.
[e] Neither Sed3Fit nor AGNFitter produced acceptable fits for 4252, so we do not list any host galaxy properties.

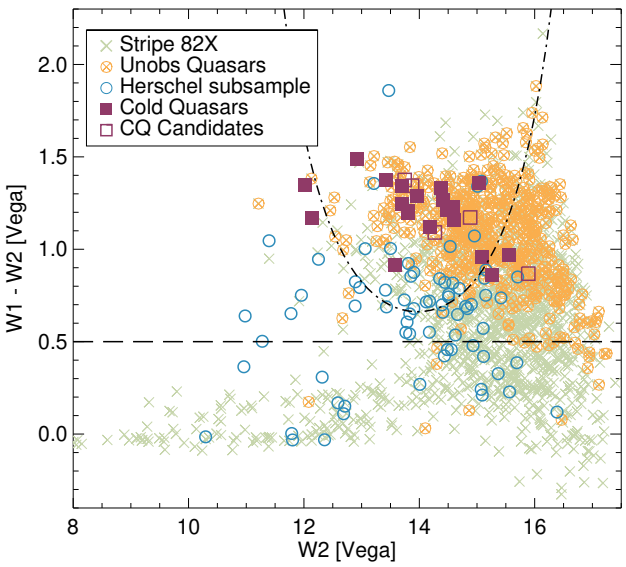

FIG. 5.— Our Stripe 82X sample in WISE colorspace. Our *Herschel* subsample (blue circles) is a mix of galaxies dominated by AGN in the mid-IR as opposed to star formation. This is expected given the range of X-ray luminosities in this sample. All the Cold Quasars (solid purple squares) and Cold Quasar candidates (unfilled purple squares) lie above dashed line, which is defined as having a 90% AGN selection completeness in (Assef et al. 2018). Most meet the more stringent 90% reliability selection (dot-dashed line) as well. From our parent Stripe 82X sample (green crosses), we plot unobscured quasars ($L_X > 10^{44}$ erg/s, $M_B < -23$) as the orange circles with crosses. The Cold Quasars are generally brighter and redder than the unobscured quasars.

criteria $W1 - W2 > 0.5$ from Assef et al. (2018), which was designed to select AGN with a completeness of 90% (dashed line; Figure 5). They also satisfy the criteria

$$W1 - W2 > 0.53 \exp[0.183(W2 - 13.76)^2] \quad (2)$$

from Assef et al. (2018), which was designed to select AGN with a reliability of 90% (dot-dashed line; Figure 5). In other words, our Cold Quasars have the near- and mid-IR emission expected of luminous AGN. A subset of mid-IR AGN are defined as hot dust-obscured galaxies (Hot DOGS; Eisenhardt et al. 2012). These are rare, dusty galaxies with $L_{\rm IR} > 10^{13}\,L_\odot$ (Wu et al. 2012). Hot DOGs are luminous quasars, yet dust obscured. Hot DOGs are also referred to as $W1W2$ dropouts due to their extremely red spectrum, and are typically selected according to $W1 > 17.4$ and $W2 - W4 > 8.2$ (Eisenhardt et al. 2012). None of our Cold Quasars meet the WISE selection criteria to be classified as Hot DOGs.

Of the parent unobscured quasar sample, 559 galaxies have $W1$ and $W2$ detections. Almost all meet the Assef et al. (2018) completeness criterion shown in Figure 5, but only 57% satisfy the reliability criterion. Our Cold Quasars lie to the upper left in the distribution of unobscured quasars in Figure 5. This means that they are in general both brighter in the near-IR ($W1$ and $W2$ trace near-IR emission at the redshifts of our sources) and redder than the average unobscured quasar in our survey. The median (standard deviation) $W1 - W2$ color of the Cold Quasars is 1.22 (0.17), while the median (standard deviation) of the unobscured quasars is 1.11 (0.27).

The Cold Quasars are also more luminous in the longer wavelength WISE bands than the unobscured quasars (Figure 6). At $z \sim 1-2$, where the majority of our Cold

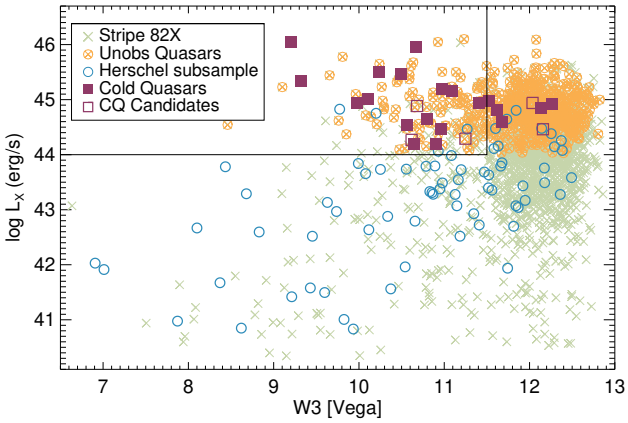

FIG. 6.— Cold Quasars (purple squares) are brighter in the longer wavelength WISE bands than typical unobscured quasars (orange circles with crosses). The full *Herschel* subsample (blue circles) has a range of $W3$ magnitudes, but many of the lower L_X sources are star-forming galaxies, which have enhanced $W3$ due to PAH emission. We recommend using $L_X > 1 \times 10^{44}$ erg/s and $W3 < 11.5$ (solid lines) to select Cold Quasar candidates.

Quasars lie, $W3$ spans $\lambda \sim 4 - 6\,\mu$m, where the torus should outshine stellar emission. Through examining our sources, we find 15 Cold Quasars (out of 20 detected in WISE) satisfy the criterion $W3 < 11.5$ [Vega]. We determined this threshold by calculating the expected $W3$ emission of infrared-selected AGN at $z = 3.2$, the redshift of the most distant Cold Quasar. We scale the IR AGN template from Kirkpatrick et al. (2012), which is empirically derived from IR AGN at $z = 1 - 3$, to $S_{250\,\mu\rm m} = 30$ mJy, the detection limit of the HerS survey, and calculate the observed $W3$ magnitude to be 11.5.

In contrast, only 19% of the unobscured quasars have $W3 < 11.5$. Combining the X-ray and optical quasar criteria with the mid-IR criterion weeds out star-forming galaxies, which can be bright in W3 at $z \sim 0 - 1$ due to the 6.2, 7.7, and 11.2 μm PAH features falling in this bandpass. In fact, many of our *Herschel* subsample show significantly enhanced W3 emission, but their low L_X ($< 10^{42}$ erg/s) and IR SED fitting indicate that they are star-forming galaxies. Due to the selection efficiency, the criteria

$$L_X > 10^{44}\,\text{erg/s} \quad (3)$$

$$M_B < -23 \quad (4)$$

$$W3 < 11.5 \quad (5)$$

can be used to select Cold Quasar candidates for longer wavelength follow-up in future surveys.

The shape of the mid-IR SED is directly related to physical properties of the torus. In a two-component model, where the torus is composed of a smooth disk surrounding by clumps of dust, the slope of the mid-IR emission depends strongly on the optical depth of the both the disk and the clumps (Siebenmorgen et al. 2015). We show the slope of the mid-IR SED, parameterized by the color $W2 - W4$ as a function of redshift in Figure 7. At $z \sim 1 - 2$, $W4$ is tracing $\lambda \sim 7 - 11\,\mu$m and $W2$ is tracing $\lambda \sim 1.5 - 2.5\,\mu$m. Cold Quasars have a bluer $W2 - W4$ color than the majority of unobscured quasars at similar redshifts. In fact, all Cold Quasars lie below the relation

$$W2 - W4 = 0.6z + 5.5 \quad (6)$$

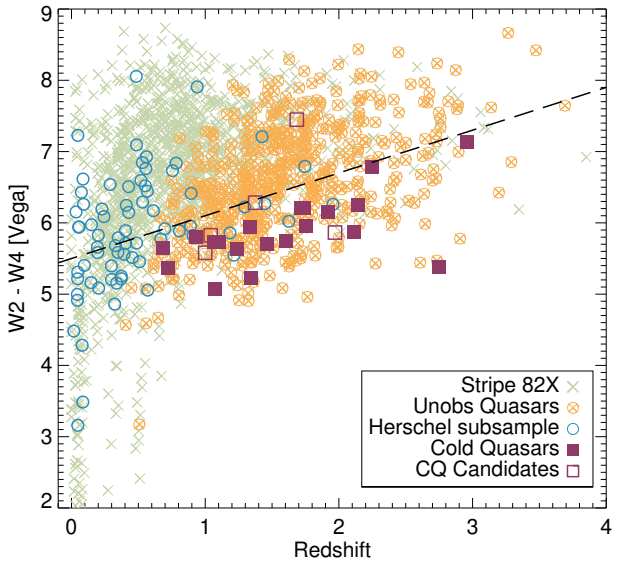

FIG. 7.— We show the slope of the mid-IR emission, parameterized as $W4-W2$, as a function of redshift. Our Cold Quasars (purple squares) have bluer colors than the unobscured quasars in the parent sample (orange circles with crosses). All Cold Quasars lie below $W2-W4=0.6z+5.5$, plotted as the dashed line. The bluer colors may be due to a torus with a small optical depth, patchy circumnuclear dust, or increasing contribution to the mid-IR colors from star-forming regions.

plotted as the dashed line. Only 40% of the unobscured quasars lie below the line. This may indicate that Cold Quasars have different torus properties, specifically with a lower optical depth, than typical unobscured quasars, or a more face-on viewing angle. Alternately, if the primary obscuring material in blue quasars is circumnuclear, rather than a torus, this indicates a low covering fraction of circumnuclear dust. Of course, sources with a lot of star formation will have bluer $W2-W4$ colors at $z\sim1-2$, as $W4$ will be tracing the continuum in between the $11.2\,\mu$m and $7.7\,\mu$m PAH peaks, while $W2$ is tracing the stellar emission, which is a maximum around $1.6\,\mu$m (Kirkpatrick et al. 2012). Cold Quasars have high star formation rates and may be expected to have a significant contribution to their mid-IR emission from star formation. We can provide a rough estimate of how much of $W2-W4$ may be due to star formation using the SED decomposition results. For those Cold Quasars fit by SED3FIT, we calculate their $W2-W4$ color from the total best fit model and from the torus component only. The torus component has a redder $W2-W4$, with the median difference in color of the sample being $\Delta\,(W2-W4)_{\rm torus-total}=0.21$. This is not enough of a difference to move the Cold Quasars above the dashed line (Equation 6). Obtaining mid-IR spectroscopy will allow us to better determine how much of the mid-IR emission is due to PAHs.

Mid-IR bright AGN in star-forming host galaxies will have significant far-IR emission attributable to the host. Kirkpatrick et al. (2013) examined the IR colors of dusty star-forming galaxies, some of which host AGN, from $z\sim1-3$. AGN are easily distinguished from star-forming galaxies using dust temperature, measured from the ratio of mid- to far-IR data. AGN-heated dust is much warmer than cool interstellar dust where stars form. With *Spitzer* and *Herschel*, the colors $S_{250\mu{\rm m}}/S_{24\mu{\rm m}}$ vs. $S_{8\mu{\rm m}}/S_{3.6\mu{\rm m}}$ reliably separate type-1 and type-2 AGN from star-forming galaxies by tracing the heating sources of the ISM and looking for hot dust from the torus, which produces a steeper continuum in AGN (Kirkpatrick et al. 2013, 2015).

In place of *Spitzer*/MIPS and IRAC observations, we use $S_{250}/W4$ to trace the ratio of cold dust to warm dust, and $W3/W1$ to trace the slope of the mid-IR continuum, and we have converted all WISE Vega magnitudes to fluxes. In the top panel of Figure 8, we show where the Cold Quasars and *Herschel* subsample lie in this colorspace. We plot the redshift tracks from $z=0.5-3.0$ of the $z\sim1$ star-forming template and featureless AGN template from Kirkpatrick et al. (2012). These templates were empirically created from 151 star-forming galaxies and AGN with *Spitzer* and *Herschel* observations at $z\sim1-3$. A few sources in our *Herschel* subsample lie in the region occupied by the star-forming template, and unsurprisingly, these are the sources with $L_X<10^{42}$ erg/s. The Cold Quasars all occupy the same region as the AGN template, while many of the *Herschel* subsample lie between the two regimes, indicated a mix of star formation and AGN emission in the mid-IR. The AGN template was derived from sources from the *Chandra* Deep Field South at $z\sim1-2$. These sources were identified as AGN on the basis of strong power-law emission in their *Spitzer*/IRS spectra. 75% have $L_{\rm IR}>10^{12}\,L_\odot$. Of these 75%, only 50% have $L_X>10^{44}$ erg/s (Brightman et al. 2014), and none meet the optical quasar definition, based on ACS photometry from the *Hubble Space Telescope* (Giavalisco et al. 2004) They are therefore a fundamentally different population than our Cold Quasars, and yet have similar ratios of far-IR emission.

We also plot a standard type-1 quasar template from Elvis et al. (1994). This template was created using the IRAS emission of UV and X-ray selected quasars, many of which are part of the Palomar-Green Survey (Green et al. 1986). Lyu & Rieke (2017) compare multiple type-1 quasar templates from the literature and determine that the templates of Elvis et al. (1994), Symeonidis et al. (2016) and Netzer et al. (2007), which are all based on the Palomar-Green Survey, accurately represent the emission of unobscured quasars, while the Kirkpatrick et al. (2012) templates are not valid for luminous type-1 objects. The Palomar-Green Survey is comprised mainly of low redshift quasars ($z<0.2$) which show a decline in far-IR emission beyond $\lambda>20\,\mu$m. However, the Elvis et al. (1994) template falls to the left of our sample, indicating that on average, low redshift unobscured quasars have much less cold dust than our Cold Quasars, which are all at $z>0.5$. In the bottom panel of Figure 8, we compare the (Elvis et al. 1994) template with the AGN and star-forming template from Kirkpatrick et al. (2012). We illustrate with the shaded regions which portion of the SED is covered by the $W1$, $W3$, $W4$, and S_{250} filters at $z=1-3$.

Our Cold Quasars demonstrate that luminous, type-1 AGN can have an abundance of cold dust, albeit only rarely. Part of the difference may be attributed to the rising gas fractions of galaxies with redshift, so that local quasar templates cannot be compared to higher redshift quasars (e.g., Geach et al. 2011; Kirkpatrick et al. 2017).

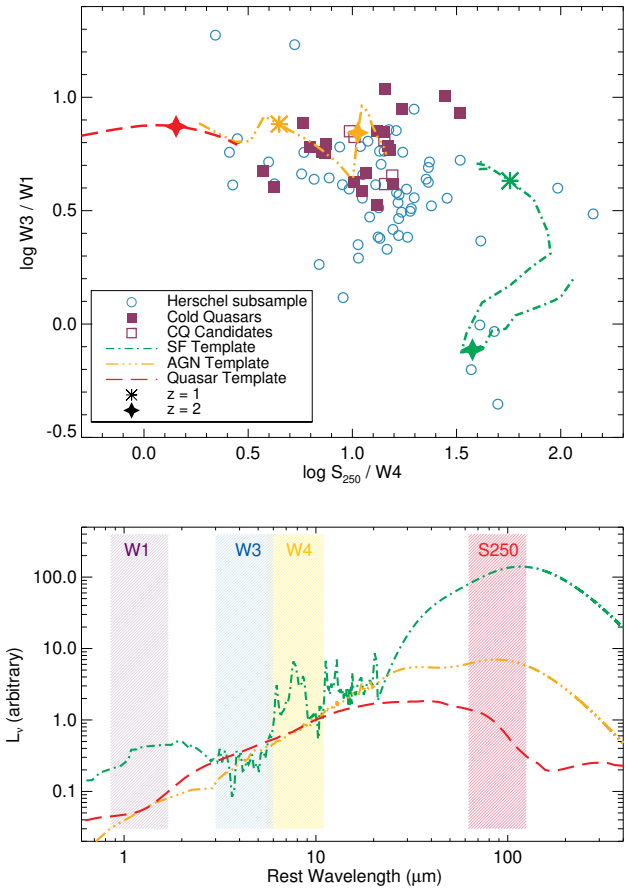

FIG. 8.— *Top panel*–$S_{250}/W4$ traces the cold to warm dust, or average dust temperature, while $W3/W1$ traces the slope of the continuum emission. We plot redshift tracks from $z = 0.5 - 3$ of a star-forming template (green dot-dashed line), AGN template (orange dot-dash-dotted line Kirkpatrick et al. 2012), and unobscured quasar template (red dashed line Elvis et al. 1994) to illustrate how star-forming galaxies separate from AGN in this color diagram. Cold Quasars (purple filled squares) have similar dust continua but warmer dust than typical unobscured quasars, as do other Herschel-detected sources (blue circles). *Bottom panel*– We visually compare the three templates plotted in the top panel, normalized at 10 μm. We illustrate with the shaded regions which portion of the SED is covered by the $W1$, $W3$, $W4$, and S_{250} filters at $z = 1 - 3$.

3.2. *Are Cold Quasars Special?*

We have defined Cold Quasars as unobscured type-1 quasars with a substantial amount of cold dust ($S_{250} > 30$ mJy). Our Cold Quasars all have intense SFRs, with the most extreme being $> 2000\,M_\odot$/yr. But, does it make sense to identify these quasars as a separate class? Answering that requires that we understand the expected amount of infrared emission in unobscured quasars, in itself a difficult question. There are 805 Stripe 82X sources with $L_X > 10^{44}$ erg/s and $M_B < -23$. Cold Quasars are 3% of this population. If we include the candidates, this rises to 4%. Based on detectability in the far-IR, Cold Quasars are indeed a special, rare population. Of course, these numbers depend sensitively on the depth of the *Herschel* data in Stripe 82, and a deeper survey may uncover more Cold Quasars. It is better to examine these quasars based on their host galaxy properties rather than satisfying an arbitrary detection threshold.

The relatively low sensitivity of *Herschel* means that only the most luminous infrared galaxies are detected with increasing redshift, even in the deepest fields (e.g. Elbaz et al. 2011). One way around *Herschel* detection limits is through stacking. Stanley et al. (2017) compile composite IR SEDs by stacking *Herschel* images and averaging *WISE* fluxes for 3000 optical SDSS unobscured AGN. They measure the average AGN bolometric luminosity, $L_{\rm Bol}$, and the average SFR from $z = 0.2-2.5$. The Stanley et al. (2017) sample is unbiased with respect to IR detections, and so we presume that their SFRs represent the typical SFR of unobscured quasars of a given bolometric luminosity. We compare our Cold Quasars with the Stanley et al. (2017) sample in the left panel of Figure 9 where we have calculated the AGN bolometric luminosity from L_X using the bolometric correction presented in Hopkins et al. (2007). Compared with the typical SFRs of unobscured quasars, our Cold Quasars having significantly higher SFRs. In the $0.8 < z < 1.5$ bin (green), the Cold Quasars have $> 4\times$ higher SFR than the typical unobscured quasars. In the $z > 1.5$ bin (red), the Cold Quasars have nearly an order of magnitude higher SFR than the unobscured quasars.

Galaxy SFR and evolution are commonly understood in the context of the main sequence, which is the tight relationship between SFR and M_* exhibited by most galaxies (Elbaz et al. 2007; Noeske et al. 2007). In the major merger paradigm, mergers trigger starbursts, significantly elevating SFR above the main sequence (Sanders & Mirabel 1996). The quasar phase is predicted to follow the starburst phase (Hopkins et al. 2007). For typical unobscured quasars, Stanley et al. (2017) find no significant difference between their SFRs and those of star-forming galaxies on the main sequence at similar redshifts. Our Cold Quasars, on the other hand, are on average 7.5× above the main sequence, parameterized by (Whitaker et al. 2012), as seen in the right panel of Figure 9. The starburst regime is typically defined to be $> 4\times$ elevated beyond the main sequence (e.g. Elbaz et al. 2011). Cold Quasars can be understood to be unobscured, type-1 quasars that lie in the starbursting regime of the main sequence. Dusty star-forming galaxies with $L_{\rm IR} = 10^{11} - 10^{12}\,L_\odot$ typically lie on the main sequence (Casey et al. 2014), which we illustrate using the median stellar mass and SFR from the dusty star-forming galaxies hosting AGN i n Kirkpatrick et al. (2012). We distinguish between those AGN that are obscured, or have clear silicate absorption, and those that are unobscured. The obscured AGN and unobscured AGN medians are from sources at $z \sim 1 - 3$ and lie around the main sequence lines. Many submillimeter galaxies are more luminous, with $L_{\rm IR} > 10^{12.5}\,L_\odot$ (e.g. Bothwell et al. 2013). We plot the median stellar mass and SFR of submillimeter galaxies from $z \sim 1 - 3$ from Bothwell et al. (2013), and these have an elevated SFR similar to our Cold Quasars.

As their SFRs are so high, we estimate how long before these quasars will exhaust their fuel supply using the dust mass, which should reliably trace the gas mass (Groves et al. 2015; Scoville et al. 2016). We plot $M_{\rm dust}$/SFR as a function of redshift in Figure 10. We compare these galaxies, which were selected in the X-ray and the IR, with a purely IR-selected sample from the literature, compiled in Kirkpatrick et al. (2019). The Kirkpatrick et al. (2019) sample is a mix of pure star-forming galaxies

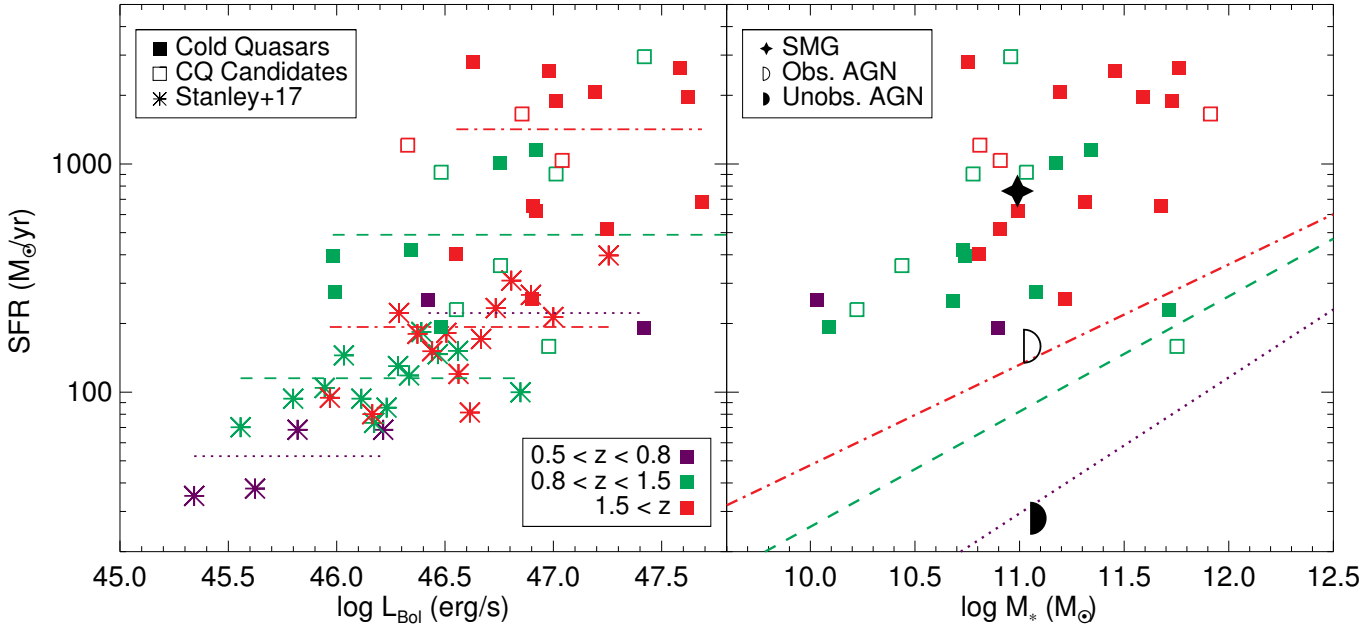

FIG. 9.— *Left*–$L_{\rm Bol}$ vs. SFR for the Cold Quasars (filled squares) and Cold Quasar candidates (unfilled squares). Colors correspond to redshift. The average SFRs of unobscured quasars from Stanley et al. (2017) are plotted as the asterisks. We plot the average SFR of the unobscured quasars and Cold Quasars in each redshift bin as the dotted and dashed lines, to help guide the eye. On average, the Cold Quasars have $> 4-9\times$ as much star formation as the unobscured quasars at the same bolometric luminosities. *Right*–M_* vs. SFR for the Cold Quasars. The dotted and dashed lines show the Whitaker et al. (2012) main sequence in the same redshift bins as in the left panel. The Cold Quasars are on average $> 7\times$ above the main sequence, squarely in the starbursting regime. For comparison, obscured AGN, and unobscured AGN at similar redshifts from Kirkpatrick et al. (2012) lie around the main sequence. The Cold Quasars have the high star formation rates typically only seen in submillimeter galaxies (SMGs), as illustrated by the median point of SMGs from Bothwell et al. (2013).

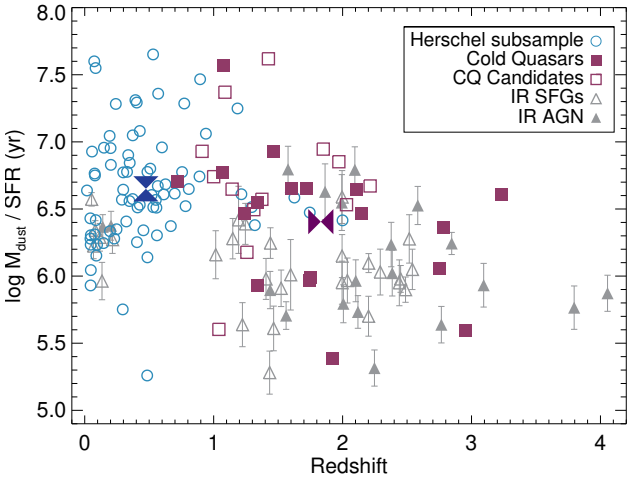

FIG. 10.— Gas depletion timescale $\tau_{\rm dep} = M_{\rm H_2}/{\rm SFR}$ as a function of redshift. We plot the Cold Quasars (purple squares) and the *Herschel* subsample (blue squares) and compare with IR selected quasars, AGN, and star forming galaxies from the literature (grey triangles). We plot the mean $\tau_{\rm dep}$ of the *Herschel* subsample as the standing bowtie and the mean $\tau_{\rm dep}$ of the Cold Quasars as the laying bowtie. The Cold Quasars have a factor of 2 shorter gas depletion time than the *Herschel* subsample.

and IR AGN in the same $L_{\rm IR}$ range as the Cold Quasars. The Cold Quasars show no offset from the IR selected sample. We use $M_{\rm dust}$ rather than $M_{\rm gas}$, as the conversion requires assumptions about the gas-to-dust ratio and generally has a high degree of scatter (Bertemes et al. 2018; Kirkpatrick et al. 2019). If we assume that the gas-to-dust ratio is 50 (where $M_{\rm gas}$ and $M_{\rm dust}$ are both measured in $M_\odot$), which has been measured in a high-redshift luminous quasar (Wang et al. 2016), then the depletion timescales range from 10 Myr – 1 Gyr. On average, the Cold Quasars have a slightly smaller depletion timescale than the *Herschel* subsample. For the *Herschel* subsample, $\log \tau_{\rm dep} = 8.35 \pm 0.05$ [yr], while for the Cold Quasars, $\log \tau_{\rm dep} = 8.10 \pm 0.12$ [yr], where we have quoted the error on the mean. This is a difference of nearly 50% in gas depletion times. However, a different conversion factor may be required for the lower luminosity sources or lower redshift sources, which would serve to enhance the difference between the Cold Quasars and the *Herschel* subsample. This could also in part be a selection effect, since the Cold Quasars are at slightly higher redshift. Galaxies at higher redshift may have higher star formation efficiencies and shorter gas depletion timescales than lower redshift galaxies (Scoville et al. 2016). We will examine the dust masses and gas depletion times of the Cold Quasars in the context of the full Stripe 82X sample in a future paper (Coleman et al., in prep). The Cold Quasars have gas depletion times that are completely consistent with the shorter gas depletion timescales observed in submillimeter galaxies, whereas normal galaxies at $z > 1$ typically have gas depletion times of 1 Gyr (Tacconi et al. 2010).

The depletion of the ISM can also occur through outflows, both from quasar winds and through supernovae winds. Fiore et al. (2017) measured molecular outflows in local Seyferts and found a correlation between AGN bolometric luminosity and mass outflow rate ($\dot{M}$), such that galaxies with $L_{\rm bol} > 10^{45}$ erg/s had $\dot{M} = 100 - 1000\, M_\odot$/yr. This translates to a mass loading factor ($\dot{M}$/SFR) of 1–100. If our Cold Quasars have

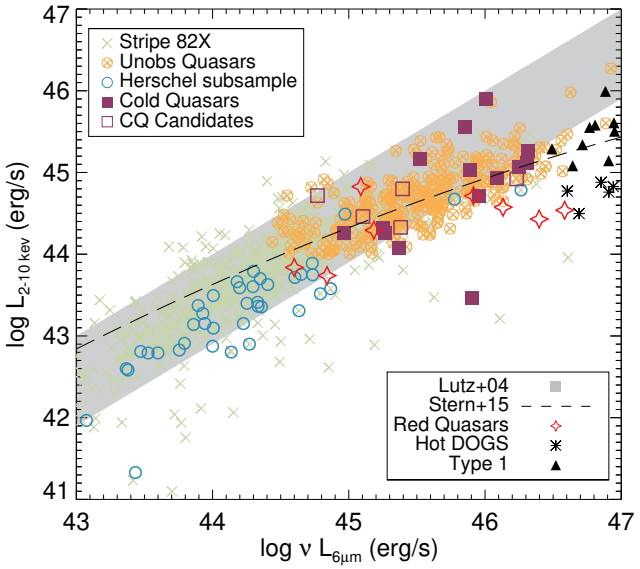

FIG. 11.— Hard X-ray luminosity as a function of 6 μm luminosity. We plot the relationship derived from local galaxies (grey shaded region), the relationship derived from higher luminosity, higher redshift sources (dashed line), and several different populations compiled in Glikman et al. (2018). The Cold Quasars predominantly follow the expected relations and have more X-ray emission relative to the Red Quasars and Hot DOGs. This indicates less gas absorption in the Cold Quasars.

similar outflows as these literature results, then their gas depletion timescales could be lower by a factor of 10 or more. In that case, these quasars may have less than ten million years left to form stars.

Finally, we consider whether Cold Quasars show the expected amount of mid-IR emission given their X-ray luminosity in Figure 11. We calculated $\nu L_{6\,\mu\mathrm{m}}$ by interpolating between the WISE fluxes. The relationship between mid-IR luminosity (parameterized by $\nu L_{6\mu\mathrm{m}}$) and hard (2-10 kev) X-ray luminosity has been quantified for local sources (Lutz et al. 2004) and high luminosity sources (Stern 2015). Sources that lie below the expected relationship (shaded region and dashed line) are underluminous in the X-ray. They can be either Compton thick or perhaps accreting above the Eddington limit, which may be the case for Hot DOGs (Ricci et al. 2017b; Wu et al. 2018). However, except for one source, our Cold Quasars lie around the expected relations derived in both Lutz et al. (2004) and Stern (2015). The outlier is source 507, which has a soft X-ray luminosity (0.5-2 keV) four times greater than the hard X-ray luminosity, but a blue optical spectrum. It is possible that the hard X-ray luminosity has been underestimated in this source. The Cold Quasars have enhanced X-ray emission compared to the Red Quasars (green stars) and Hot DOGs (black asterisks) from LaMassa et al. (2017); Glikman et al. (2017, 2018), particularly at $\nu L_6 > 10^{46}$ erg/s. However, they follow the same trend as type-1 quasars (black triangles; Glikman et al. 2018). νL_6 traces the amount of hot dust from the torus, while L_X is sensitive to gas absorption. For a given νL_6, Cold Quasars have less gas absorption than Red Quasars. Similar to the Red Quasars, local merging ultra luminous galaxies are also underluminous in the X-rays compared with the infrared, indicating a high degree of absorption attributable to the merger (Teng et al. 2015).

In the major merger framework, obscured quasars are understood to be a specific phase of a massive galaxy's life right before blowout (Hopkins et al. 2007; Kocevski et al. 2015; Glikman et al. 2015). Tidal tails and train wreck merger signatures are still visible in Red Quasars, which have gas absorption visible through lower X-ray emission and redder optical continua (Glikman et al. 2015). High gas column densities are also observed in local major mergers of massive dusty galaxies, many of which harbor obscured AGN (Petric et al. 2011; Teng et al. 2015). On the other hand,Dai et al. (2014) identify a large population of blue broad-line quasars at $z \sim 1-3$ detected at 24 μm which have clear merger signatures, illustrating that mergers do not universally obscure the central AGN.

Within the merging paradigm, the rare Cold Quasars we have defined are perhaps in a critical transition phase where the AGN growth co-exists peacefully within a starbursting galaxy for a brief epoch before quenching. Cold Quasars may immediately follow the Red Quasar stage, where a quasar wind has swept through the inner galaxy, removing the dust, but has not yet reached the star forming outskirts. However, Cold Quasars have slightly higher SFRs than what has been measured in Red Quasars. Urrutia et al. (2012) measure an average SFR of $\sim 100\,M_\odot$/yr in Red Quasars at $z < 1$, with a couple of Red Quasars having SFR$\sim 10\,M_\odot$/yr. This introduces a tension to Cold Quasars following the Red Quasar phase, although Cold Quasars could have more positive feedback.

Crucial to understanding the evolutionary stage of Cold Quasars is understanding where the dust lies and the morphology of the host galaxy. ALMA observations of submillimeter galaxies at $z \sim 2-3$ have revealed that the dust is compact, more so than the gas, mainly lying within 1–3 kpc of the galaxy center (Hodge et al. 2016; Rujopakarn et al. 2016; Hodge et al. 2019; Rujopakarn et al. 2019). If the same is true for Cold Quasars, then perhaps the quasar has managed to punch a hole in the dust, producing a blue color. In that case, Cold Quasars may simply be patchy Red Quasars, rather than a separate evolutionary phase altogether. Red Quasars have clear merger signatures, so one way to test this hypothesis is to obtain sensitive observations of the ISM, where the quasar will not outshine the host galaxy, and look for disturbed morphological features. Currently, the spatial extent of submillimeter emission from quasars is unknown. ALMA observations of the spatial distribution of the ISM in these galaxies is required to both look for fueling signatures, such as tidal tails, and determine the location of the dust and gas.

If indeed Red Quasars, Cold Quasars, and Blue Quasars are linked together in an evolutionary sequence, the life cycle may be 3-4% of the blue quasar phase, which is loosely constrained to be 10^6-10^9 yr (Conroy & White 2013; La Plante & Trac 2016). For comparison, the Red Quasar phase is 20% of the blue quasar phase (Glikman et al. 2012). We have based our estimation on considering only those unobscured quasars that lie in the same redshift range as our Cold Quasars. Tighter constraints can be placed with a mass-matched sample, but we currently lack stellar mass estimates for the full Stripe 82X catalog. If the blue quasar phase lasts a Gyr, then Cold Quasars may last only 40 Myr, which is consistent with

the estimate based on the star formation efficiency in Figure 10.

4. CONCLUSIONS

We present a rare sample of X-ray and optically selected broad-line quasars that are detected in all three *Herschel*/SPIRE bands. We define Cold Quasars to be broad-line AGN with $L_X > 10^{44}\,\mathrm{erg/s}$, $M_B < -23$, and $S_{250} > 30\,\mathrm{mJy}$. Our findings are:

1. Cold Quasars and Cold Quasar candidates comprise 4% of the unobscured quasar population in Stripe 82X. If understood through the merger-driven paradigm, the duration may be 4% of the blue quasar phase.

2. Cold Quasars have enhanced mid-IR emission relative to most unobscured quasars. $W3 < 11.5\,[\mathrm{Vega}]$ is an efficient mid-IR selection criteria for Cold Quasar candidates, selecting 75% of our Cold Quasars but only 19% of the full unobscured quasar population. This implies they have considerably more dust and possibly less circumnuclear obscuration than typical unobscured quasars.

3. Cold Quasars also have a bluer mid-IR spectra than the average unobscured quasar, and the color $W4 - W2$ can also be used to select Cold Quasar candidates. This blue color may be due to a torus with a lower optical depth than is typical of unobscured quasars, or it may be due to contamination of the mid-IR by the strong star formation emission in these galaxies.

4. Cold Quasars have significantly more cold dust, as traced by $S_{250\,\mu\mathrm{m}}$, than expected based on lower redshift unobscured quasars. The amount of cold dust is consistent with that measured in mid-IR selected AGN at $z \sim 1-2$. The cold dust can be attributed to star formation, and Cold Quasars have unusually high SFRs of $200 - 2000\,M_\odot/\mathrm{yr}$.

5. The immense SFRs of Cold Quasars are $4-7\times$ higher than the average unobscured quasar at the same redshift. Cold Quasars lie off the main sequence and qualify as starburst galaxies. Whether these immense AGN luminosities and SFRs are triggered by major mergers will require high resolution submm follow-up with ALMA.

6. Cold Quasars are best defined as blue type-1 quasars that exist in starbursting galaxies.

This exciting population of unobscured quasars with significant amounts of cold dust could represent an transition phase between dust-obscured quasars and unobscured quasars that have already depleted their interstellar medium. Further observations of the ISM will provide a more complete picture of how close these sources are to quenching.

This research is based upon work supported by NASA under award No. 80NSSC18K0418 to Yale University and by the National Science Foundation under Grant No. AST-1715512. E.T. acknowledges support from FONDECYT Regular 1160999 and 1190818, CONICYT PIA ACT172033 and Basal-CATA AFB170002 grants. A.K. gratefully acknowledges support from the YCAA Prize Postdoctoral Fellowship. E.G. acknowledges the generous support of the Cottrell College Award through the Research Corporation for Science Advancement.

REFERENCES

Ananna, T. T., Salvato, M., LaMassa, S., et al. 2017, ApJ, 850, 66
Ananna, T. T., Treister, E., Urry, C. M., et al. 2019, ApJ, 871, 240
Arnouts, S., Cristiani, S., Moscardini, L., et al. 1999, MNRAS, 310, 540
Assef, R. J., Stern, D., Noirot, G., et al. 2018, ApJS, 234, 23
Azadi, M., Coil, A. L., Aird, J., et al. 2017, ApJ, 835, 27
Baldwin, J. A., Phillips, M. M., & Terlevich, R. 1981, PASP, 93, 5
Berta, S., Lutz, D., Santini, P., et al. 2013, A&A, 551, A100
Bertemes, C., Wuyts, S., Lutz, D., et al. 2018, MNRAS, 478, 1442
Bothwell, M. S., Smail, I., Chapman, S. C., et al. 2013, MNRAS, 429, 3047
Brandt, W. N., Alexander, D. M., Hornschemeier, A. E., et al. 2001, AJ, 122, 2810
Brightman, M., Nandra, K., Salvato, M., et al. 2014, MNRAS, 443, 1999
Bruzual, G., & Charlot, S. 2003, MNRAS, 344, 1000
Buchner, J., & Bauer, F. E. 2017, MNRAS, 465, 4348
Buchner, J., Schulze, S., & Bauer, F. E. 2017, MNRAS, 464, 4545
Calistro Rivera, G., Lusso, E., Hennawi, J. F., & Hogg, D. W. 2016, ApJ, 833, 98
Cappelluti, N., Hasinger, G., Brusa, M., et al. 2007, ApJS, 172, 341
Casey, C. M., Narayanan, D., & Cooray, A. 2014, Phys. Rep., 541, 45
Ciotti, L., & Ostriker, J. P. 2007, ApJ, 665, 1038
Civano, F., Marchesi, S., Comastri, A., et al. 2016, ApJ, 819, 62
Conroy, C., & White, M. 2013, ApJ, 762, 70
da Cunha, E., Charlot, S., & Elbaz, D. 2008, MNRAS, 388, 1595
Dai, Y. S., Elvis, M., Bergeron, J., et al. 2014, ApJ, 791, 113
Dey, A., Schlegel, D. J., Lang, D., et al. 2019, AJ, 157, 168
Donley, J. L., Koekemoer, A. M., Brusa, M., et al. 2012, ApJ, 748, 142
Eisenhardt, P. R. M., Wu, J., Tsai, C.-W., et al. 2012, ApJ, 755, 173
Elbaz, D., Daddi, E., Le Borgne, D., et al. 2007, A&A, 468, 33
Elbaz, D., Dickinson, M., Hwang, H. S., et al. 2011, A&A, 533, A119
Elitzur, M., & Shlosman, I. 2006, ApJ, 648, L101
Elvis, M., Wilkes, B. J., McDowell, J. C., et al. 1994, ApJS, 95, 1
Elvis, M., Civano, F., Vignali, C., et al. 2009, ApJS, 184, 158
Fiore, F., Feruglio, C., Shankar, F., et al. 2017, A&A, 601, A143
Flaugher, B., Diehl, H. T., Honscheid, K., et al. 2015, AJ, 150, 150
Fliri, J., & Trujillo, I. 2016, MNRAS, 456, 1359
Fritz, J., Franceschini, A., & Hatziminaoglou, E. 2006, MNRAS, 366, 767
Geach, J. E., Smail, I., Moran, S. M., et al. 2011, ApJ, 730, L19
Giacconi, R., Zirm, A., Wang, J., et al. 2002, ApJS, 139, 369
Giavalisco, M., Ferguson, H. C., Koekemoer, A. M., et al. 2004, ApJ, 600, L93
Glikman, E., Gregg, M. D., Lacy, M., et al. 2004, ApJ, 607, 60
Glikman, E., LaMassa, S., Piconcelli, E., Urry, M., & Lacy, M. 2017, ApJ, 847, 116
Glikman, E., Simmons, B., Mailly, M., et al. 2015, ApJ, 806, 218
Glikman, E., Urrutia, T., Lacy, M., et al. 2012, ApJ, 757, 51
—. 2013, ApJ, 778, 127
Glikman, E., Lacy, M., LaMassa, S., et al. 2018, ApJ, 861, 37
Goulding, A. D., Alexander, D. M., Bauer, F. E., et al. 2012, ApJ, 755, 5
Green, R. F., Schmidt, M., & Liebert, J. 1986, ApJS, 61, 305
Groves, B., Dopita, M., & Sutherland, R. 2006, A&A, 458, 405

Groves, B. A., Schinnerer, E., Leroy, A., et al. 2015, ApJ, 799, 96
Hainline, K. N., Hickox, R. C., Chen, C.-T., et al. 2016, ApJ, 823, 42
Hainline, K. N., Shapley, A. E., Greene, J. E., & Steidel, C. C. 2011, ApJ, 733, 31
Hatziminaoglou, E., Hernán-Caballero, A., Feltre, A., & Piñol Ferrer, N. 2015, ApJ, 803, 110
Heckman, T. M., & Best, P. N. 2014, ARA&A, 52, 589
Hickox, R. C., Jones, C., Forman, W. R., et al. 2009, ApJ, 696, 891
Hodge, J. A., Swinbank, A. M., Simpson, J. M., et al. 2016, ApJ, 833, 103
Hodge, J. A., Smail, I., Walter, F., et al. 2019, ApJ, 876, 130
Hopkins, P. F., Hernquist, L., Cox, T. J., & Kereš, D. 2008, ApJS, 175, 356
Hopkins, P. F., Richards, G. T., & Hernquist, L. 2007, ApJ, 654, 731
Hopkins, P. F., Somerville, R. S., Hernquist, L., et al. 2006, ApJ, 652, 864
Ilbert, O., Arnouts, S., McCracken, H. J., et al. 2006, A&A, 457, 841
Imanishi, M., Nakanishi, K., & Izumi, T. 2016, AJ, 152, 218
Jester, S., Schneider, D. P., Richards, G. T., et al. 2005, AJ, 130, 873
Jiang, L., Fan, X., Bian, F., et al. 2014, ApJS, 213, 12
Kamenetzky, J., Rangwala, N., Glenn, J., Maloney, P. R., & Conley, A. 2016, ApJ, 829, 93
Kirkpatrick, A., Pope, A., Sajina, A., et al. 2015, ApJ, 814, 9
Kirkpatrick, A., Sharon, C., Keller, E., & Pope, A. 2019, arXiv e-prints, arXiv:1905.06961
Kirkpatrick, A., Pope, A., Alexander, D. M., et al. 2012, ApJ, 759, 139
Kirkpatrick, A., Pope, A., Charmandaris, V., et al. 2013, ApJ, 763, 123
Kirkpatrick, A., Alberts, S., Pope, A., et al. 2017, ApJ, 849, 111
Kocevski, D. D., Brightman, M., Nandra, K., et al. 2015, ApJ, 814, 104
La Plante, P., & Trac, H. 2016, ApJ, 828, 90
Lacy, M., Storrie-Lombardi, L. J., Sajina, A., et al. 2004, ApJS, 154, 166
LaMassa, S. M., Urry, C. M., Glikman, E., et al. 2013a, MNRAS, 432, 1351
LaMassa, S. M., Urry, C. M., Cappelluti, N., et al. 2013b, MNRAS, 436, 3581
—. 2013c, MNRAS, 436, 3581
LaMassa, S. M., Cales, S., Moran, E. C., et al. 2015, ApJ, 800, 144
LaMassa, S. M., Urry, C. M., Cappelluti, N., et al. 2016, ApJ, 817, 172
LaMassa, S. M., Glikman, E., Brusa, M., et al. 2017, ApJ, 847, 100
Lawrence, A., Warren, S. J., Almaini, O., et al. 2007, MNRAS, 379, 1599
Lutz, D., Maiolino, R., Spoon, H. W. W., & Moorwood, A. F. M. 2004, A&A, 418, 465
Lyu, J., & Rieke, G. H. 2017, ApJ, 841, 76
Mahoro, A., Pović, M., & Nkundabakura, P. 2017, MNRAS, 471, 3226
Marchesi, S., Civano, F., Elvis, M., et al. 2016, ApJ, 817, 34
Mateos, S., Alonso-Herrero, A., Carrera, F. J., et al. 2012, MNRAS, 426, 3271
McDowell, J. C., Elvis, M., Wilkes, B. J., et al. 1989, ApJ, 345, L13
McMahon, R. G., Banerji, M., Gonzalez, E., et al. 2013, The Messenger, 154, 35
Mullaney, J. R., Alexander, D. M., Goulding, A. D., & Hickox, R. C. 2011, MNRAS, 414, 1082
Netzer, H., Lutz, D., Schweitzer, M., et al. 2007, ApJ, 666, 806
Noeske, K. G., Weiner, B. J., Faber, S. M., et al. 2007, ApJ, 660, L43
Papovich, C., Shipley, H. V., Mehrtens, N., et al. 2016, ApJS, 224, 28
Perna, M., Sargent, M. T., Brusa, M., et al. 2018, A&A, 619, A90
Petric, A. O., Armus, L., Howell, J., et al. 2011, ApJ, 730, 28
Pontzen, A., & Governato, F. 2012, MNRAS, 421, 3464
Ricci, C., Assef, R. J., Stern, D., et al. 2017a, ApJ, 835, 105
—. 2017b, ApJ, 835, 105
Rosario, D. J., Santini, P., Lutz, D., et al. 2012, A&A, 545, A45
Rujopakarn, W., Dunlop, J. S., Rieke, G. H., et al. 2016, ApJ, 833, 12
Rujopakarn, W., Daddi, E., Rieke, G. H., et al. 2019, arXiv e-prints, arXiv:1904.04507
Sajina, A., Yan, L., Fadda, D., Dasyra, K., & Huynh, M. 2012, ApJ, 757, 13
Salomé, Q., Salomé, P., & Combes, F. 2015, A&A, 574, A34
Sanders, D. B., & Mirabel, I. F. 1996, ARA&A, 34, 749
Schmidt, M., & Green, R. F. 1983, ApJ, 269, 352
Schulze, A., Silverman, J. D., Daddi, E., et al. 2019, arXiv e-prints, arXiv:1906.04290
Scoville, N., Aussel, H., Brusa, M., et al. 2007, ApJS, 172, 1
Scoville, N., Sheth, K., Aussel, H., et al. 2016, ApJ, 820, 83
Shangguan, J., & Ho, L. C. 2019, ApJ, 873, 90
Siebenmorgen, R., Heymann, F., & Efstathiou, A. 2015, A&A, 583, A120
Silva, L., Maiolino, R., & Granato, G. L. 2004, MNRAS, 355, 973
Spoon, H. W. W., Marshall, J. A., Houck, J. R., et al. 2007, ApJ, 654, L49
Stanley, F., Alexander, D. M., Harrison, C. M., et al. 2017, MNRAS, 472, 2221
Stern, D. 2015, ApJ, 807, 129
Stern, D., Eisenhardt, P., Gorjian, V., et al. 2005, ApJ, 631, 163
Stern, D., Assef, R. J., Benford, D. J., et al. 2012, ApJ, 753, 30
Stierwalt, S., Armus, L., Surace, J. A., et al. 2013, ApJS, 206, 1
Symeonidis, M., Giblin, B. M., Page, M. J., et al. 2016, MNRAS, 459, 257
Tacconi, L. J., Genzel, R., Neri, R., et al. 2010, Nature, 463, 781
Teng, S. H., Rigby, J. R., Stern, D., et al. 2015, ApJ, 814, 56
Timlin, J. D., Ross, N. P., Richards, G. T., et al. 2016, ApJS, 225, 1
Treister, E., Schawinski, K., Urry, C. M., & Simmons, B. D. 2012, ApJ, 758, L39
Treister, E., Urry, C. M., Chatzichristou, E., et al. 2004, ApJ, 616, 123
Urrutia, T., Lacy, M., & Becker, R. H. 2008, ApJ, 674, 80
Urrutia, T., Lacy, M., Spoon, H., et al. 2012, ApJ, 757, 125
Urry, C. M., & Padovani, P. 1995, PASP, 107, 803
Viero, M. P., Asboth, V., Roseboom, I. G., et al. 2014, ApJS, 210, 22
Wang, R., Wu, X.-B., Neri, R., et al. 2016, ApJ, 830, 53
Whitaker, K. E., van Dokkum, P. G., Brammer, G., & Franx, M. 2012, ApJ, 754, L29
Wu, J., Tsai, C.-W., Sayers, J., et al. 2012, ApJ, 756, 96
Wu, J., Jun, H. D., Assef, R. J., et al. 2018, ApJ, 852, 96